Gold Nanostructures

Deutsche Ausgabe: DOI: 10.1002/ange.201503996
Internationale Ausgabe: DOI: 10.1002/anie.201503996

# Octahedral and Cubic Gold Nanoframes with Platinum Framework**

*Songyi Ham, Hee-Jeong Jang, Yookyung Song, Kevin L. Shuford,* and Sungho Park**

**Abstract:** *Herein, we report a general synthetic pathway to various shapes of three-dimensional (3D) gold nanoframes (NFs) embedded with a Pt skeleton for structural rigidity. The synthetic route comprises three steps: site-specific (edge and vertex) deposition of Pt, etching of inner Au, and regrowth of Au on the Pt framework. Site-specific reduction of Pt on Au nanoparticles (NPs) led to the high-quality of 3D Au NFs with good structural rigidity, which allowed the detailed characterization of the corresponding 3D metal NFs. The synthetic method described here will open new avenues toward many new kinds of 3D metal NFs.*

Controlling the shape of noble-metal nanostructures has attracted enormous attention because it allows tailoring of their optical properties[1,2] enabling the nanostructures suitable for the applications, for example, as catalysts,[3] biosensors,[4] substrates for surface-enhanced Raman scattering,[5] and photothermal therapy agents.[6] Among many metal nanostructures, Au NFs[7–10] are particularly interesting compared to analogous solid NPs, because their inner space can be utilized to enhance the permeability of chemicals and light, resulting in improved catalytic activity[11] and an enhanced electromagnetic field,[12] respectively. Au NFs are commonly synthesized with limited success by the galvanic replacement reaction[13–15] between Ag NPs and Au ions. In the synthetic strategy, the morphology of Ag NPs dictates the final shape of the resultant Au NFs. However, it is still required to develop general synthetic pathways for NFs with a good controllability of composition, rim-thickness, size, and shape homogeneity.[16]

Herein, we report the synthesis of 3D Au NFs (octahedral and cubic structures as proof-of-concept) and their corresponding optical properties. Our results indicate that our proposed synthesis strategy is not limited to specific shapes. Additionally, the Au NFs showed good stability under chemically harsh environments such as $O_2$ plasma treatment and extreme pH conditions, which is a critical requirement for the application of 3D NFs as sensors, catalysts, and photothermal therapy agents. We attributed their outstanding stability to the presence of an inner hard Pt skeleton that supported the entire nanostructure.

We synthesized octahedral 3D Au NFs with a Pt skeleton through site-specific (edge and vertex) deposition of Pt on octahedral Au NPs, etching of inner Au, and regrowth of Au on the Pt skeleton, as shown in Figure S1. First, octahedral Au NPs were prepared as starting materials and Pt was selectively reduced on the edges and vertexes of the octahedral Au NPs (site-specific deposition step). The mechanism of rim-preferential growth of Pt is described in our previous report.[17] Briefly, a thin Ag layer was formed on the Au octahedral NPs by adding trace amounts of $AgNO_3$ and ascorbic acid. This thin layer of Ag played an important role in the selective deposition of Pt at the edges, which was facilitated by electron shuttling through oxidation and reduction processes of the Ag layer. When $Pt^{4+}$ ions were added, Pt atoms were selectively reduced at the edges and vertexes through a galvanic replacement reaction between the Ag layer and $Pt^{4+}$ ions. Exclusive deposition of Pt at those facets was more favorable than on flat terraces, probably due to the higher surface energy of the edge and vertex as compared to the terrace. The coordination number of a flat terrace site is nine, whereas edge and vertex sites have lower coordination numbers ($CN_{\mathrm{edge}} \approx 8$, $CN_{\mathrm{vertex}} \approx 6$).[18] A lower coordination number implies more available reaction sites, indicating more reactive facets. Second, the inner Au part of the octahedral Au@Pt NPs was selectively etched to $Au^{+}$ by the addition of $Au^{3+}$ ions, resulting in Pt octahedral NFs (etching step). Finally, addition of ascorbic acid to the solution induced the reduction of $Au^{+}$ ions on the Pt skeleton (regrowth step), leading to octahedral 3D Au NFs.

We characterized the morphology of the resultant octahedral Au NPs (Figure 1A), octahedral Au@Pt NPs (Figure 1B), octahedral Pt NFs (Figure 1C), and octahedral Au NFs (Figure 1D) in detail using field emission scanning electron microscopy (FESEM). Each low-magnification image shows the homogeneity of the NPs and NFs in terms of size and shape. The corresponding high magnification SEM images are exhibited from panels (E) to (H), respectively, showing their dimensions and morphologies in detail (corresponding to panels (I)–(L)). Pure octahedral Au NPs had a well-defined smooth surface morphology (panel E). When the surface was coated with Pt, it is clearly noticeable that the selective deposition of Pt occurred on edges and vertexes, generating eight craters. The edge length (62 ± 5 nm) of octahedral Au NPs increased to 90 ± 9 nm after Pt deposition. Typically, the Pt rim thickness was 27 ± 3 nm and the thickness could be controlled by the amount of $Pt^{4+}$ ions added. The addition of $Au^{3+}$ ions selectively etched out the inner Au component, as clearly exhibited in panel G, which shows only

---

[*] S. Ham,[+] H.-J. Jang,[+] Y. Song, Prof. S. Park
Department of Chemistry, Sungkyunkwan University
Suwon 440-746 (South Korea)
E-mail: spark72@skku.edu
Prof. K. L. Shuford
Department of Chemistry and Biochemistry, Baylor University
Waco, TX, 76798 (USA)
E-mail: kevin_shuford@baylor.edu

[+] These authors contributed equally to this work.

[**] K.L.S. was supported by the Chemical Sciences, Geosciences, and Biosciences Division, Office of Basic Energy Sciences, Office of Science, U.S. Department of Energy, under award number DE-SC0010212. S. Park thanks for financial support from the National Research Foundation of Korea (National Leading Research Lab: NRF-2011-0027911, Pioneer Research Center: 2012-0009586).

Supporting information for this article is available on the WWW under http://dx.doi.org/10.1002/anie.201503996.

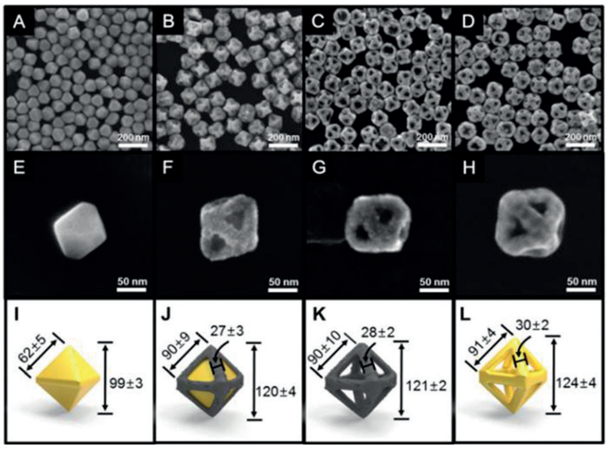

***Figure 1.*** FESEM images of A) octahedral Au NPs, B) octahedral Au@Pt NPs, C) octahedral Pt NFs, and D) octahedral Au NFs. High-magnification SEM images (E to H) corresponding to panels (A) to (D). Dimensions of each octahedral nanostructure are shown in panels (I) to (L); all scales in nm. Scale bars (A–D) = 200 nm; scale bars (E–H) = 50 nm.

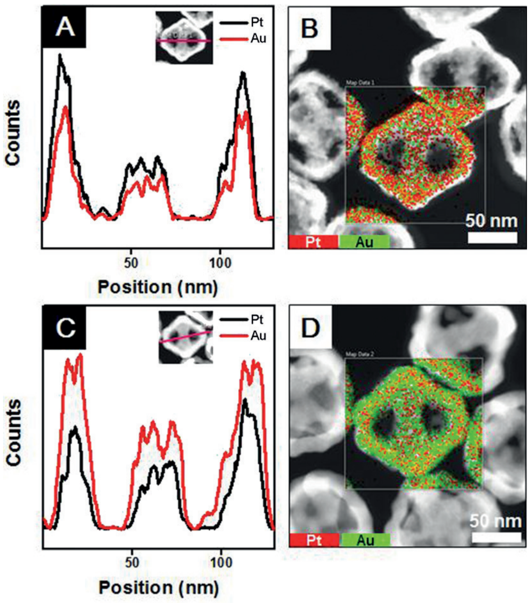

***Figure 2.*** EDS line and image mapping of octahedral Pt NFs (A and B) and octahedral Au NFs (C and D). The black line represents the amount of Pt, and the red line is that of Au. The line mapping scanned along the red line in inset. In the image mapping, red dots indicate Pt, and green dots correspond to Au after coating with ca. 1.0 nm Au.

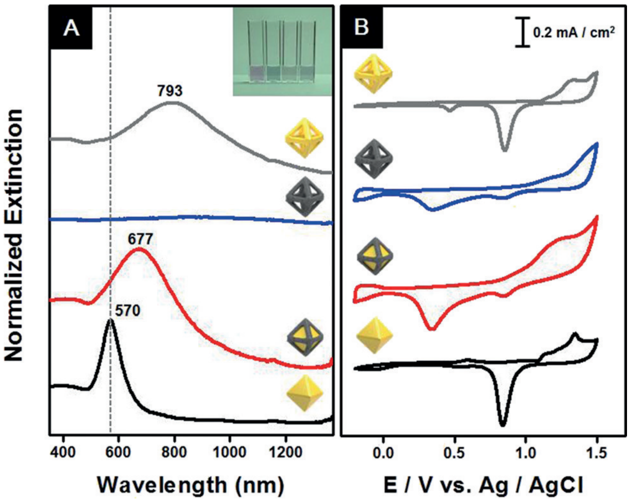

***Figure 3.*** a) UV/Vis-NIR spectra and B) cyclic voltammograms show the octahedral Au NPs (black line), octahedral Au@Pt NPs (red-line), octahedral Pt NFs (blue line), and octahedral Au NFs (grey line). Inset photograph image indicates octahedral Au NPs (pink), octahedral Au@Pt NPs (blue), octahedral Pt NFs (colorless), and octahedral Au NFs (bluish-grey). 0.1 M $H_2SO_4$ was used as electrolyte in all CVs (with a scan rate of 50 $mVs^{-1}$).

Pt NFs. During etching, the optical band (at 270 nm) of $Au^{3+}$ ions dampened, indicating the conversion of core Au and etchant $Au^{3+}$ to $Au^{+}$ ions (Figure S2). There were no noticeable changes in the physical dimensions of Pt NFs compared to Au@Pt NPs (panels J and K). Finally, $Au^{+}$ ions were reduced on the Pt NFs by addition of ascorbic acid, leading to Au NFs. The rim thickness of octahedral Au NFs increased gradually during the regrowth of Au; accordingly, the peak of Au octahedral NFs was blueshifted during the regrowth of Au (Figure S3). In general, Au NFs were larger than Pt NFs, indicating a slight increase in rim-thickness from 28 ± 2 to 30 ± 2 nm (Figure 1, panel L). EDS line and image mappings clearly indicate a dominant Pt and Au surface composition before and after Au coating, respectively (Figure 2). Typically, the atomic fractions of Pt and Au after Au coating are 31.66 % and 68.34 %, respectively (Figure S4).

The shape evolution was monitored by time-resolved UV/Vis-NIR spectroscopy, and the typical final spectral profiles are represented in Figure 3, panel A, corresponding to SEM images in Figure 1. Each octahedral nanostructure had unique colors due to their different surface plasmon resonance characteristics. Inset photograph image indicated each sample dispersed in water. Au octahedral NPs had a typical dipole window, oscillation of surface-free electrons on the Au surface induced collective oscillation of surface-free electrons of Pt, and therefore the Au@Pt octahedral NP behaved optically as larger Au octahedral NPs through surface plasmon coupling between Au and Pt, as indicated by the redshift of the peak. This optical coupling is consistent with theoretical calculations. After selective etching of the gold component in the octahedral Au@Pt NPs, no noticeable surface plasmon band originated from the octahedral pure Pt NFs, because Pt is optically almost inactive in the investigated spectral window, as mentioned above (blue line). However, the octahedral Au NFs exhibited a unique surface plasmon peak at 793 nm after the regrowth of Au on the octahedral Pt NFs (grey line). In comparison with octahedral pure Au NPs, the octahedral Au NFs had two unique features. First, the peak was drastically redshifted from 570 to 793 nm. Analysis of SEM images revealed that the height (124 ± 4 nm) of 3D Au NFs is much larger than that (99 ± 3 nm) of octahedral Au NPs. The increase in size and formation of a hollow interior in the 3D Au NFs contributed to the shift of the peak to a longer wavelength. Additionally, surface-free electrons on the narrow rims of 3D Au NFs induced field-induced polarizations more readily than solid octahedral Au NPs (i.e., it was easier for the 3D Au NFs to polarize), which resulted in redshifts of the plasmon modes. This is consistent with the lightening-rod effect in elongated NPs, in which large fields reside in the highly curved tips and the plasmon resonances shift to longer wavelengths. In addition to redshifts, we found that the 3D Au NFs had broader resonance widths than solid octahedral Au NPs. Broader widths implies an increase in the damping rate, likely due to a slight inhomogeneity in rim size and electron-interface scattering.

To determine the surface composition of the various nanostructures, we performed electrochemical characterization by measuring cyclic voltammograms (CVs) in acidic electrolyte (Figure 3, panel B). Octahedral pure Au NPs had a wide double layer region below ca. 0.7 V and there was anodic formation of oxide above 1.3 V and cathodic removal of oxide at 0.9 V. After modification of the edges and vertexes of octahedral Au NPs with Pt, the CV shows two new features evident below 0.5 V, representing the anodic–cathodic current profile that consists of near-reversible peaks associated with hydrogen adsorption–desorption (−0.2 V to 0.0 V), and an irreversible feature appeared at 0.4 V corresponding to the removal of surface Pt oxide. In the case of octahedral Pt NFs, the trace cathodic feature at 0.9 V is due to the presence of Au residue on Pt octahedral NFs after selective etching of the inner Au component. After coating with Au, the complete removal of reversible features below 0.0 V indicated near-complete coating of the Pt NFs with Au.

We computed the NP spectra using discrete dipole approximation (DDA). The optical properties of stratified shell structures are very sensitive to morphology. To simplify the analysis, we modeled a single morphology and varied the material components to extract spectral trends. Size parameters were based on the experimentally determined dimensions (Figure 1).

Figure 4 displays the computed optical spectra. The Au octahedron (Figure 4 A, black trace) shows a single peak at 600 nm. This is in good agreement with experiment and consistent with previous modeling studies on Au octahedra.[19] Adding a Pt frame to the Au octahedron core (Figure 4 A, red trace) shifts the resonance slightly but considerably broadens the peak width. The experimental spectrum (Figure 3 A, red trace) shows the broadening effect but is red-shifted by ca. 100 nm. However, if a calculation is performed on the exact same structure entirely composed of Au (Figure 4 A, purple trace), the computed spectrum is consistent with experiments for the octahedral Au@Pt NP (i.e., one obtains a broadened peak effectively acting like Au. A uniform Au shell morphology with a hollow center (Figure 4 A, green trace) yields a narrower, more intense resonance that is red-shifted, analogous to the trends in concentric spheres.

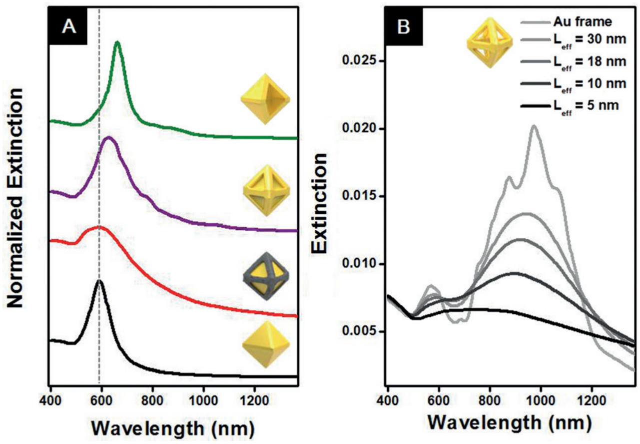

***Figure 4.*** A) UV/Vis-NIR spectra obtained from DDA calculation; solid octahedral Au NPs (black line), octahedral Au@Pt NPs (red line), octahedral Au@Au NPs (purple line), and hollow octahedral Au nanoshell (green line). B) UV/Vis-NIR spectra of octahedral Au NFs with varying effective scattering length ($L_{eff}$).

The value of the bulk permittivity used in the calculations can be corrected to account for electron-surface scattering (see the Supporting Information). Without corrections, the Au NF yields a complex spectrum showing multiple peaks, which originates from narrow Au regions that couple readily to one another and the incident field. The experimental trace in Figure 3 A does not display these complex features; the resonance is broad and blue-shifted from the uncorrected DDA result. Figure 4 B shows that decreasing the effective scattering length ($L_{eff}$) generates decreased intensities, peak broadening, and a net blueshift of major spectral features. This general trend is notably more consistent with experiment, suggesting that surface scattering is significant in the hollow Au NFs. From the calculations and comparison with experiment, the effective scattering length for these NPs is likely in the 5–10 nm range, which is larger than the thinnest regions of the frame but notably smaller than the thickest.

A significant feature of the Au octahedral NFs was their structural rigidity, which was endowed by the inner Pt skeleton. To explore the structural stability of Au octahedral NFs, we exposed the NFs to harsh environments such as $O_2$ plasma treatment (Figure S5) and extreme pH conditions (Figure S6). Under these conditions, Au nanoshells without a Pt skeleton that were synthesized through galvanic replacement between Ag NPs and $Au^{3+}$ ions usually aggregated or collapsed structurally. In contrast, the octahedral Au NFs retained their original morphology without any noticeable alterations; we believe that this is because the Pt skeleton supported the entire structure.

It is important to point out that our suggested strategy to synthesize Au NFs is not limited to octahedral NFs. We applied site-specific deposition and etching-regrowth processes to cubic Au nanostructures to demonstrate the synthesis of cubic Au NFs, as shown in Figure 5 A. It has been reported that Au nanocubes are comprised of six large-area (100) facets and eight small-area (111) facets.[20,21] Selective growth of Pt could successfully occur along edges and the formation of Pt islands on (100) facets was additionally observed, as clearly indicated in the SEM images shown in panels (B) to (E). In a previous study that investigated the site-specific overgrowth of Pt on Au facets, Pt overgrowth was shown to occur more efficiently on (100) facets than (111) facets.[22] During selective etching of the inner Au component, most Pt islands on the (100) facets were removed, and the resulting cubic Pt NFs had a unique morphology, clearly representing eight little holes that were originally (111) facets

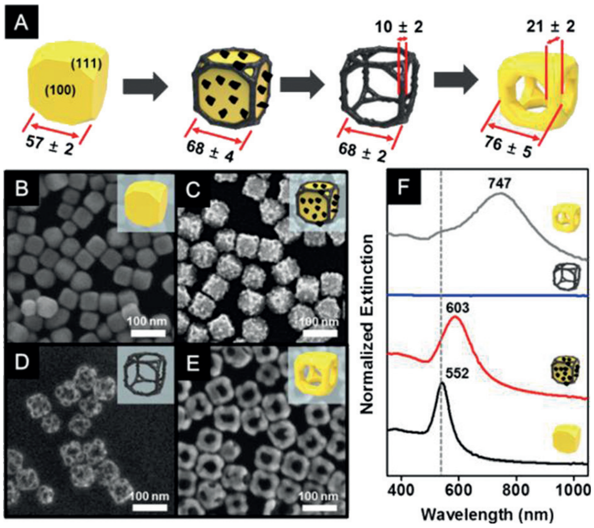

*Figure 5.* A) Illustration and dimensions (nm) of each cubic nanostructure. FESEM images show B) the cubic Au NPs, C) cubic Au@Pt NPs, D) cubic Pt NFs, and E) cubic Au NFs. F) UV/Vis-NIR spectra showing the peak position of each cubic nanostructure.

of the Au cubes. Six (100) facets were converted into large holes. The addition of ascorbic acid to a solution containing cubic Pt NFs and $Au^+$ ions triggered the reduction of $Au^+$ along the rims of the Pt NFs and resulted in the formation of cubic Au NFs. The high quality of nanostructures allowed us to characterize their unique surface plasmon resonance bands as represented in panel F. Given that there are many examples regarding the synthesis of Au NPs with different shapes, our synthetic strategy could potentially be used to convert differently shaped Au NPs into novel Au NFs.

In conclusion, we successfully synthesized octahedral and cubic 3D Au NFs through selective deposition of Pt on edges and vertexes followed by an Au etching/regrowth process. The resulting samples showed high homogeneity in terms of size and shape, which allowed detailed characterization of corresponding surface plasmon bands. The synthesis strategy proposed for Au NFs in this study may allow the creation of unprecedented nanostructures with applications in optical, biomedical, and catalytic fields.

**Keywords:** gold · nanoframes · nanoparticles · platinum · surface plasmon resonance

**How to cite:** *Angew. Chem. Int. Ed.* **2015**, *54*, 9025–9028
*Angew. Chem.* **2015**, *127*, 9153–9156

---

[1] Q. Zhang, J. Xie, J. Y. Lee, J. Zhang, C. Boothroyd, *Small* **2008**, *4*, 1067–1071.
[2] C. J. Orendorff, T. K. Sau, C. J. Murphy, *Small* **2006**, *2*, 636–639.
[3] L.-F. Zhang, S.-L. Zhong, A.-W. Xu, *Angew. Chem. Int. Ed.* **2013**, *52*, 645–649; *Angew. Chem.* **2013**, *125*, 673–677.
[4] E. M. Larsson, J. Alegret, M. Käll, D. S. Sutherland, *Nano Lett.* **2007**, *7*, 1256–1263.
[5] M. A. Mahmoud, M. A. El-Sayed, *J. Am. Chem. Soc.* **2010**, *132*, 12704–12710.
[6] J. Chen, D. Wang, J. Xi, L. Au, A. Siekkinen, A. Warsen, Z.-Y. Li, H. Zhang, Y. Xia, X. Li, *Nano Lett.* **2007**, *7*, 1318–1322.
[7] J. Chen, J. M. McLellan, A. Siekkinen, Y. Xiong, Z.-Y. Li, Y. Xia, *J. Am. Chem. Soc.* **2006**, *128*, 14776–14777.
[8] M. McEachran, D. Keogh, B. Pietrobon, N. Cathcart, I. Gourevich, N. Coombs, V. Kitaev, *J. Am. Chem. Soc.* **2011**, *133*, 8066–8069.
[9] G. S. Métraux, Y. C. Cao, R. Jin, C. A. Mirkin, *Nano Lett.* **2003**, *3*, 519–522.
[10] M. M. Shahjamali, M. Bosman, S. Cao, X. Huang, X. Cao, H. Zhang, S. S. Pramana, C. Xue, *Small* **2013**, *9*, 2880–2886.
[11] M. A. Mahmoud, M. A. El-Sayed, *Nano Lett.* **2011**, *11*, 946–953.
[12] A. Gopalakrishnan, M. Chirumamilla, F. De Angelis, A. Toma, R. P. Zaccaria, R. Krahne, *ACS Nano* **2014**, *8*, 7986–7994.
[13] W. Zhang, J. Yang, X. Lu, *ACS Nano* **2012**, *6*, 7397–7405.
[14] X. Hong, D. Wang, S. Cai, H. Rong, Y. Li, *J. Am. Chem. Soc.* **2012**, *134*, 18165–18168.
[15] D. Wan, X. Xia, Y. Wang, Y. Xia, *Small* **2013**, *9*, 3111–3117.
[16] H.-J. Jang, S. Ham, J. A. I. Acapulco, Y. Song, S. Hong, K. L. Shuford, S. Park, *J. Am. Chem. Soc.* **2014**, *136*, 17674–17680.
[17] H.-J. Jang, S. Hong, S. Park, *J. Mater. Chem.* **2012**, *22*, 19792.
[18] S. Park, S. A. Wasileski, M. J. Weaver, *J. Phys. Chem. B* **2001**, *105*, 9719–9725.
[19] C. Li, K. L. Shuford, M. Chen, E. J. Lee, S. O. Cho, *ACS Nano* **2008**, *2*, 1760–1769.
[20] X. Kou, Z. Sun, Z. Yang, H. Chen, J. Wang, *Langmuir* **2009**, *25*, 1692–1698.
[21] L. Au, Y. Chen, F. Zhou, P. H. C. Camargo, B. Lim, Z.-Y. Li, D. S. Ginger, Y. Xia, *Nano Res.* **2008**, *1*, 441–449.
[22] M. Min, C. Kim, Y. I. Yang, J. Yi, H. Lee, *Phys. Chem. Chem. Phys.* **2009**, *11*, 9759.

Received: May 1, 2015